

# Tripling of the Superconducting Critical Current Density in $\text{BaFe}_2(\text{As}_{1-x}\text{P}_x)_2$ Retained After Pressure Release

Jiangteng Liu

*Department of Electrical & Computer Engineering, University of Washington, Seattle, WA*

Alex Lopez

*Department of Mechanical Engineering, University of California Los Angeles, Los Angeles, CA 90095*

Zhaoyu Liu and Jiun-Haw Chu

*Department of Physics, University of Washington, Seattle, WA 98195*

Serena Eley

*Department of Electrical & Computer Engineering, University of Washington, Seattle, WA 98195*

(Dated: January 6, 2026)

Superconducting performance is tunable not only via chemical modification or defect engineering, but also through external parameters such as pressure, though this method remains less readily accessible. In this work, we study how compression influences vortex dynamics and critical currents in an iron-based superconductor. Specifically, we perform magnetization measurements using an off-the-shelf pressure cell to investigate the effects of hydrostatic pressures up to 1.08 GPa on the magnetic properties of  $\text{BaFe}_2(\text{As}_{0.62}\text{P}_{0.38})_2$  crystals across a range of temperatures  $T$  and magnetic fields  $H$ . Although these pressures minimally affect the superconducting critical temperature, they produce a clear increase in the critical current density  $J_c(T, H)$ , a pronounced reduction in the rate of thermally activated vortex motion  $S(T, H)$ , and can change the dominant vortex pinning mechanism. Furthermore, the effects of pressure are irreversible: after pressurization and subsequent release at room temperature, the crystals retain their enhanced critical current densities. The second magnetization peak vanishes at 22 K after the pressure cycle, which we attribute to a transition from predominantly  $\delta\kappa$  pinning to a mixed mechanism of  $\delta T_c$  and surface pinning. Lastly, a threefold increase in  $J_c$  and more than 40% reduction in  $S$  at 8 K and 0.5 T was achieved after 1–2 pressure cycles. These findings demonstrate the potential utility of pressure cycling for improving  $J_c$ , which may offer a simpler alternative to approaches such as chemical doping or the introduction of artificial pinning centers.

## I. INTRODUCTION

Pressure is an effective tool for tuning superconductivity, with the potential to enhance transition temperatures, alter orbital overlap, adjust electron-phonon coupling strength, suppress competing magnetic orders, and induce structural transitions that give rise to new phases [1–9]. In many systems, applied pressure mimics the effects of chemical doping, as both strain the lattice and alter electronic structure, providing a clean, reversible route to probe structure–property relationships without introducing chemical disorder.

Even modest compressive strains of a few gigapascals may strongly enhance superconductivity. For example, in FeSe applying only 1.48 GPa drives the  $T_c$  from 9 K to 27 K [10] possibly due to enhanced antiferromagnetic spin fluctuations [11]. Importantly, superconducting performance in applications is governed not only by transition temperature but also by the motion of vortices — penetrating magnetic flux lines whose dynamics directly determine the critical current density  $J_c$ . Defects and doping can pin vortices, suppressing their motion and thereby enhancing  $J_c$ , making vortex physics central to both fundamental understanding and technological optimization.

In fact, pressure has been shown to improve vortex pinning and the critical current density [12, 13], for example, in  $\text{Fe}_{1-x}\text{Co}_x\text{Se}_{0.5}\text{Te}_{0.5}$  [14, 15]. Despite these promising effects, maintaining high pressure during normal operation is impractical for most real-world applications, motivating strategies that can preserve pressure-induced improvements after pressure release. For example, recent interest has arisen in the pressure-quench protocol (PQP), in which superconductors retain pressure-induced structural modifications after pressure release, potentially stabilizing enhanced states at ambient conditions [16, 17]. However, pressure must be released at low temperatures, which requires custom pressure cells.

In this work, we employ an off-the-shelf pressure cell to study iron-based superconductors, focusing on two questions: how applied pressure influences  $J_c$  and thermally activated vortex motion (creep parameter  $S$ ), and whether these crystals can preserve pressure-induced enhancements after release. This approach probes the role of lattice strain in vortex dynamics and superconducting performance, while assessing the practicality of using a compact, off-the-shelf pressure cell and room-temperature release as a pathway toward engineering improved superconductors.

## II. RESULTS AND DISCUSSION

We studied the effects of hydrostatic pressure on two overdoped, superconducting  $\text{BaFe}_2(\text{As}_{0.62}\text{P}_{0.38})_2$  single crystals (sample #1 and #2) grown using a self-flux technique. Growth detail is included in the Methods section. In particular, we determined the pressure dependence of the critical current density  $J_c(T, H)$  and rate of thermally activated vortex motion  $S(T, H)$  from magnetization studies conducted over a range of temperature  $T$  and magnetic fields  $H$ . Because magnetometry also detects the signal from the sample mount — which is especially substantial for a pressure cell — meticulous background subtraction protocols, described below, are requisite for accurate results.

### Pressure cell characterization

All measurements of the magnetic moment  $m$  were collected using a Quantum Design MPMS3 magnetometer, with the sample mounted either on a standard brass sample holder or inside an off-the-shelf BeCu pressure cell capable of reaching pressures up to 1.3 GPa. For pressure-dependent measurements, the sample was loaded into a Teflon capsule with an outer diameter of 2.6 mm and an inner diameter of 2.2 mm, as illustrated in Fig. 1(a). The pressure was calibrated using a tin (Sn) manometer, as the critical temperature  $T_c$  of pure Sn exhibits a linear pressure dependence of  $dP/dT_c = -0.489$  GPa/K in the range 0 – 1.3 GPa. The tin piece was placed directly adjacent to the sample to ensure that the measured pressure accurately reflects the pressure experienced by the crystal. The pressure-dependent  $T_c$  of the tin manometer is shown in Supplementary Fig. S1.

The pressure cell introduces a large background signal (e.g., 0.015 emu at 4 K and 7 T) that varies strongly with both temperature and magnetic field, as shown in Fig. 1(b). In particular, the field dependence becomes markedly nonlinear at low temperatures. These complex features make accurate background subtraction essential to determine the true sample moment.

The Quantum Design MPMS-3 software *MultiVu* determines the magnetic moment by fitting the measured voltage  $V(z)$ , obtained as the sample is scanned through a second-order gradiometer pickup coil set, to the theoretical dipole response function, where  $z$  denotes the sample position relative to the center of the coil set [18–21]:

$$V(z) = A \left\{ \frac{2}{(R^2 + z^2)^{3/2}} - \frac{1}{[R^2 + (z + L)^2]^{3/2}} - \frac{1}{[R^2 + (z - L)^2]^{3/2}} \right\} + V_0 \quad (1)$$

Here,  $R$  is the gradiometer radius,  $L$  is the gradiometer half length, and  $V_0$  is the voltage offset. The resulting

fitted dipole amplitude  $A$  is then converted to a magnetic moment via a fixed calibration constant. Therefore, background subtraction on the extracted moment can only be performed if the background itself follows a dipolar response. However, as shown in Fig. 1(c), the magnetic background of the pressure cell does not exhibit a dipole-like shape, and thus the subtraction must instead be carried out at the raw voltage–position stage. Figure 1(d) presents the voltage–position scans of the sample prior to background subtraction. This data was collected at 18 K with the magnetic field swept up and down (0 T to 7 T to 0 T). The dipole fits (blue curves) are noticeably poor matches with the data. By comparison, Fig. 1(e) shows the corrected scans after background subtraction, where a reliable dipole fit can be achieved, yielding an accurate magnetic moment for the sample. Note that, because the sample volume is much smaller than the pressure cell chamber volume, a filler material is required to achieve the designed pressure. In our measurements, we used a Teflon spacer as the filler. This configuration may introduce a non-uniform pressure environment, resulting in the sample experiencing heterogeneous pressure during the measurement.

### Effect of pressurization on vortex pinning

To investigate the effect of hydrostatic pressure on the superconducting state of overdoped  $\text{BaFe}_2(\text{As}_{1-x}\text{P}_x)_2$ , we measured the magnetic moment against temperature under pressures ranging from 0 to 1.08 GPa in both zero field cooling (ZFC) and field cooling (FC) conditions, as shown in Fig. 2(a). With increasing pressure, the superconducting transition shifts progressively to lower temperatures. Because this shift is relatively small, we extracted  $T_c$  using multiple criteria to ensure that the trend is reliable.

The pressure dependence of the onset transition temperature  $T_c^{\text{onset}}$  is summarized in Fig. 2(b). We used two methods to determine  $T_c^{\text{onset}}$ : (1) a ZFC criterion, defined as the temperature where the normalized moment decreases below  $-0.02$ , and (2) a ZFC-FC criterion, defined as the temperature at which the difference between the ZFC and FC curves exceeds 0.02 of the normalized moment. Apart from this, we also extracted the offset transition temperature  $T_c^{\text{offset}}$ , defined as the temperature where the normalized moment falls below  $-0.98$ , as shown in Fig. 2(c). As expected for overdoped compositions, the extracted  $T_c$  decreases with increasing pressure [22, 23]. The only deviation occurs at the 0 GPa point in the onset analysis. We attribute this anomaly to non-homogeneous pressurization caused by the filler material used inside the pressure chamber.

We next examined the temperature-dependent critical current density  $J_c(T)$  under different applied pressures. Here,  $J_c$  was calculated using the Bean critical

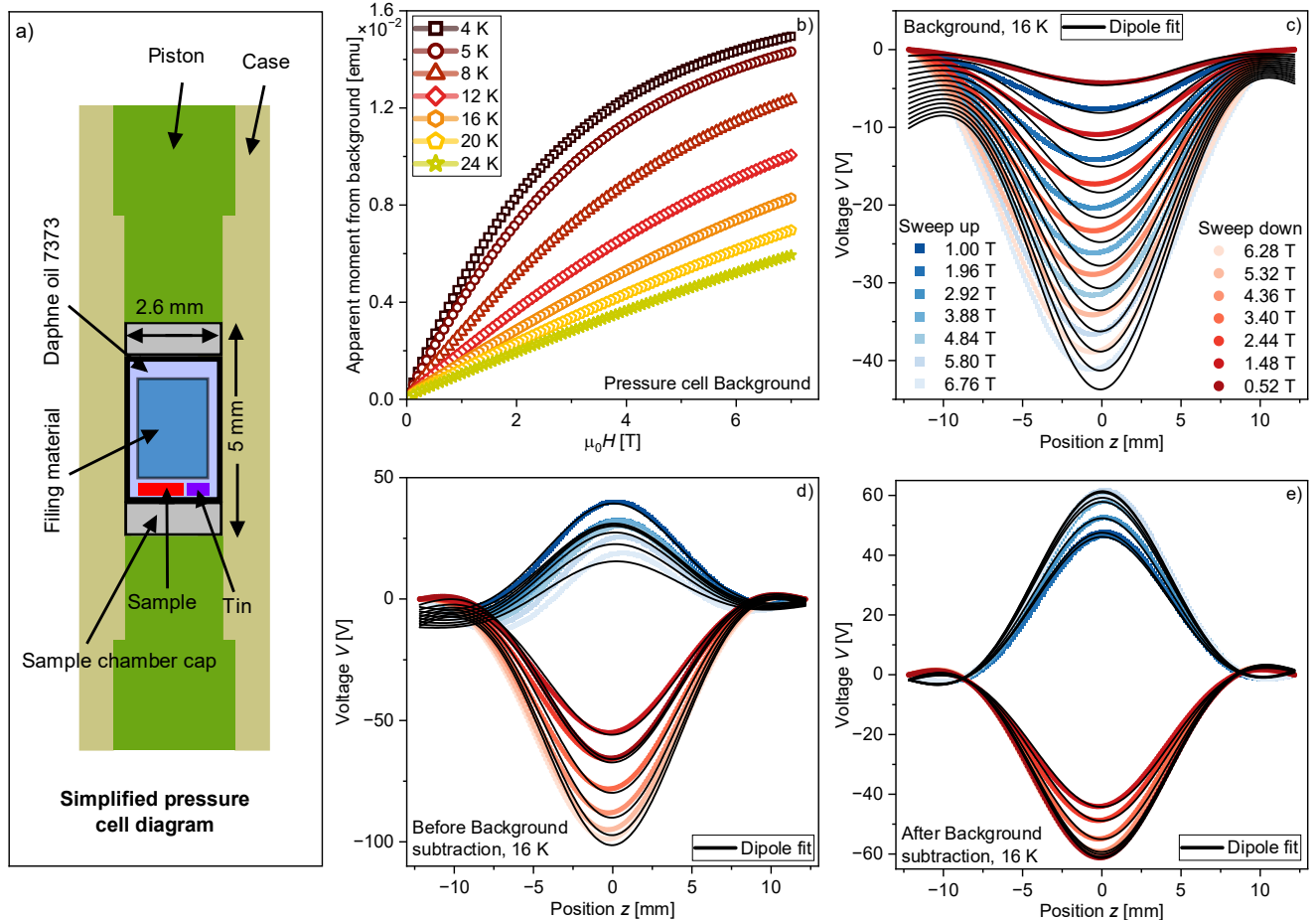


FIG. 1. (a) Schematic of the Quantum Design MPMS 3 pressure cell. (b) Field-dependent background moment of the pressure cell measured at different temperatures. The “apparent moment” refers to the moment parameter returned by the dipole fit applied to a non-dipolar background response. (c–e) Selected voltage vs position raw scans at 16 K for sweep up and down (0–7–0 T) the magnetic field. The black curve indicates the dipole fit. (c) Pure background signal. (d) Combined background and sample signal before background subtraction. (e) Sample signal after background subtraction.

state model for rectangular samples [24, 25],

$$J_c(T) = \frac{20 \Delta m(T)}{w^2 l \delta \left(1 - \frac{w}{3l}\right)}, \quad (2)$$

where  $\Delta m$  is the difference in moment between the upper and lower branches of the hysteresis loop, and  $w$ ,  $l$ , and  $\delta$  denote the width, length, and thickness of the crystal, respectively. Here,  $J_c$ ,  $m$ , the geometric dimensions, and the prefactor 20 carry units of  $\text{A cm}^{-2}$ , emu, cm, and  $\text{A cm}^{-2} \text{emu}^{-1}$ , respectively.

Figure 3(a) shows the temperature dependence of  $J_c$  for Sample #1 at an applied field of 0.5 T during pressurization. As expected,  $J_c$  decreases monotonically with increasing temperature. When comparing different pressures, the 0 GPa curve exhibits the lowest  $J_c$ , while all pressures above 0 GPa yield similar  $J_c$  values, indicating only a weak pressure dependence, as summarized in

the insert. We find that the sample volume decreases after pressurization. Because the geometric dimensions cannot be measured *in situ* during the pressure cycle, a constant volume was assumed for all pressures in the Bean model calculation. As a result, the  $J_c$  values shown for  $P > 0$  GPa are slightly underestimated. The exact dimensions used are provided in Supplementary Table S1.

Many competing interactions dictate vortex dynamics, determining the rate of thermally-activated vortex motion (creep) and  $J_c$ . This includes vortex pinning by inhomogeneities in the free energy landscape (caused by defects or strain), vortex elasticity, vortex–vortex interactions, anisotropy, thermal fluctuations, and current-driven forces [26–28]. Pinning lowers the vortex core energy by  $U_P$ , while applied currents tilt the energy landscape [29], reducing the effective barrier to a current-dependent form  $U(J)$ . Considering the ef-

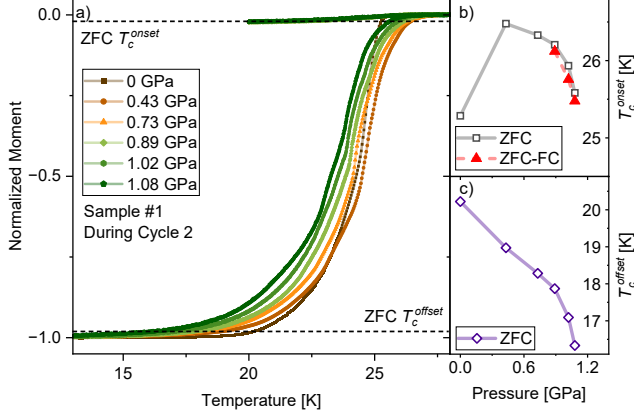


FIG. 2. (a) Normalized magnetic moment as a function of temperature for sample #1 during the second pressurization cycle. Here, an applied field of  $H = 10$  Oe was used at 0 GPa, while  $H = 3$  Oe was used for all subsequent pressures. (b) Pressure dependence of  $T_c^{onset}$ , where  $T_c^{onset}$  values were extracted using two approaches: ZFC-only, and the difference between the ZFC and FC curves. (c) Pressure dependence of  $T_c^{offset}$ .

fects of current, temperature, and magnetic field, the activation barrier  $U_{act}(T, H, J)$  follows an Arrhenius law  $t = t_0 e^{U_{act}(J)/k_B T}$ , where  $1/t_0$  is related to the attempt frequency estimated at  $10^6$ – $10^{10}$  Hz [30–33]. Collective creep theory predicts that

$$U_{act}(J) = \frac{U_p}{\mu} \left[ \left( \frac{J_c}{J} \right)^\mu - 1 \right], \quad (3)$$

where the glassy exponent  $\mu$  characterizes the size and dimensionality of vortex bundles that hop during the creep process (e.g. single flux lines, small or large bundles of size less than or greater than the penetration depth) [26, 28]. This framework predicts logarithmic decay in the induced current density and corresponding magnetization

$$J(t) \propto M(t) \approx M_0 \left[ 1 + \frac{\mu k_B T}{U_p} \ln \left( \frac{t}{t_0} \right) \right]^{-1/\mu}. \quad (4)$$

We can directly measure this decay in the magnetization, caused by vortex creep and termed magnetic relaxation, by repeatedly recording the magnetic moment  $m(t) \propto M(t)$  over time. From this, we can extract the vortex creep parameter as follows:

$$S \equiv \left| \frac{d \ln M}{d \ln t} \right| = \frac{k_B T}{U_0 + \mu k_B T \ln(t/t_0)}. \quad (5)$$

Figure 3(b) displays  $S(T)$  during pressurization. Within the temperature range of 4–8 K,  $S$  systematically decreases with increasing pressure. This decreasing trend is more clearly illustrated in the insert, where both

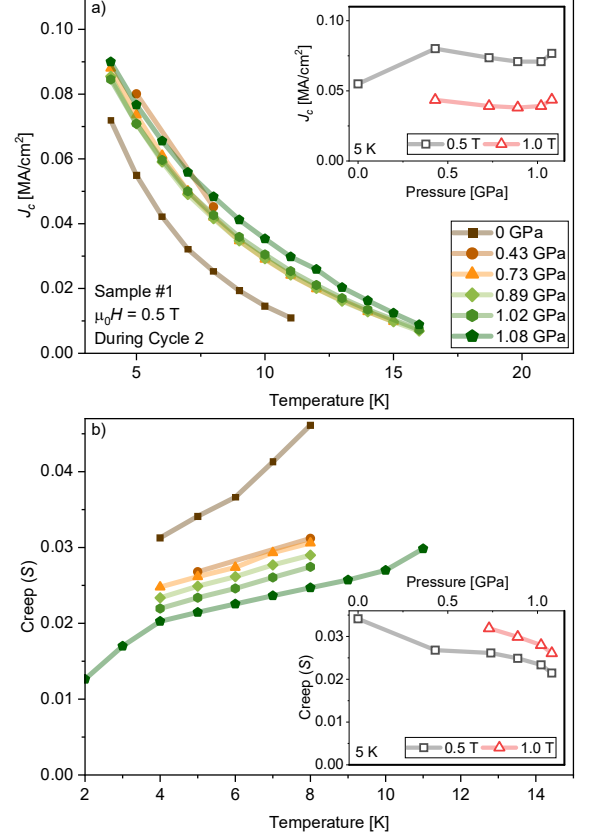


FIG. 3. Temperature-dependent (a) critical current density and (b) vortex creep parameter  $S$  for sample #1 during pressurization. The insert shows the pressure dependence of  $J_c$  and  $S$  under different applied magnetic fields at 5 K. The data presented here is from the second pressurization cycle.

the 0.5 T and 1 T datasets exhibit a similar pressure dependence. The temperature dependence of  $J_c$  and  $S$  at  $\mu_0 H = 1$  T is presented in Supplementary Fig. S4.

### Effect of pressure cycling on vortex pinning

When performed at low temperature, the PQP protocol has shown that pressure-induced structural modifications can be retained after pressure release at low temperatures, leading to significant enhancements in  $T_c$ . Here, we study whether similar irreversible effects can occur on P-doped Ba122 crystals when pressurization and depressurization occur at room temperature. To test this, the sample was pressurized from 0 GPa to 1.08 GPa and then released back to ambient pressure. We then measured the magnetization, hysteresis, and magnetic relaxation before and after the pressure cycle.

In sample #1, we noticed that the pressurization process was irreversible, in that the  $T_c$  and  $J_c$  did not return

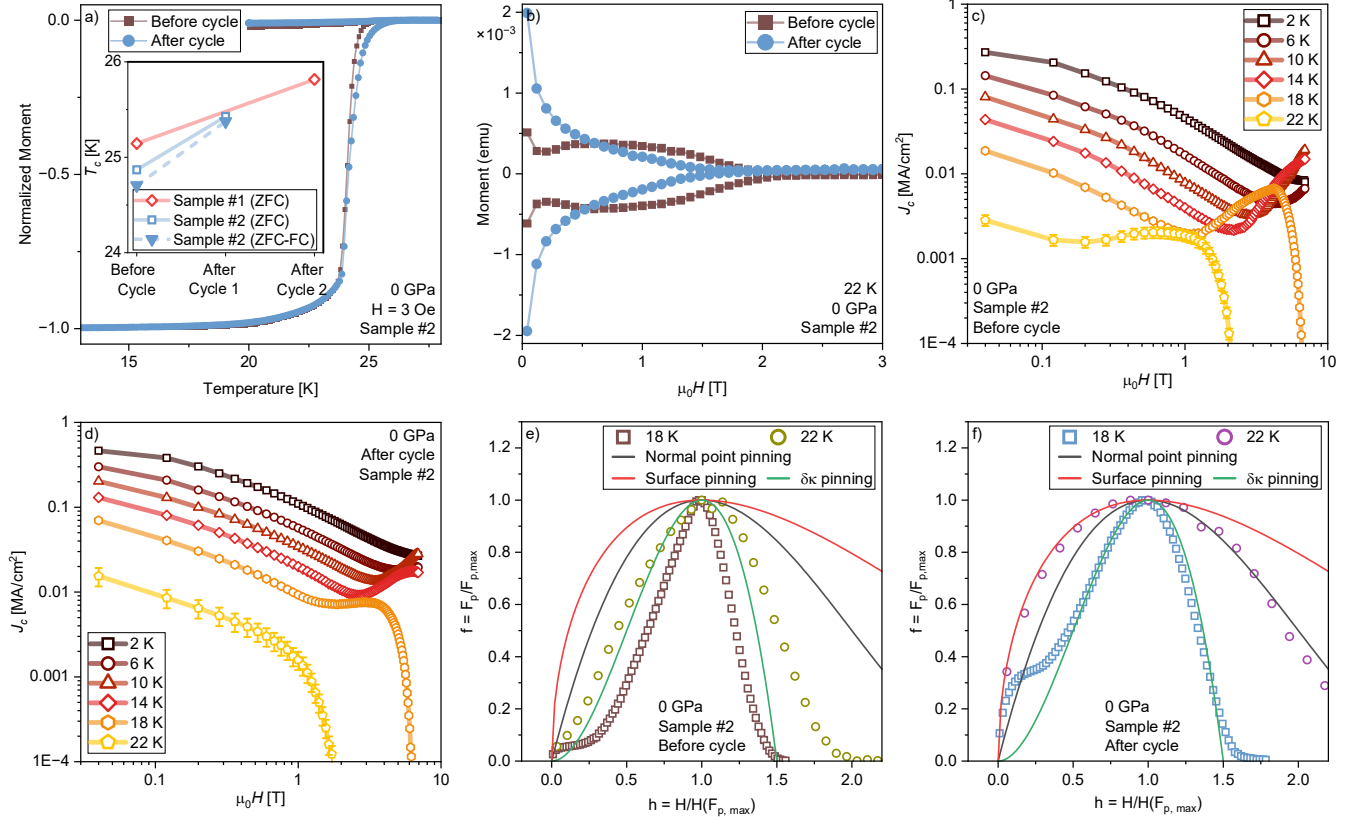


FIG. 4. (a) Normalized magnetic moment as a function of temperature for sample #2 before and after the first pressurization cycle and release back to ambient pressure. The inset shows the effect of the pressure cycle on  $T_c$  for both sample #1 and sample #2, where  $T_c$  values were extracted using two approaches: ZFC-only, and from the difference between the ZFC and FC curves. For sample #1, the peak pressure achieved in cycles 1 and 2 is 0.60 and 1.08 GPa, respectively. For sample #2 the peak pressure achieved after the cycle is 1.08 GPa. (b) Effect of the pressure cycle on the magnetic hysteresis loop of sample #2 at 22 K. Field-dependent  $J_c$  for sample #2 measured (c) before and (d) after the pressure cycle at different temperatures. Normalized pinning force  $f = F_p/F_{p,max}$  against reduced field  $h = H/H(F_{p,max})$  at 18 and 22 K for (e) before and (f) after the pressure cycle.

to their original values after pressure release. To systematically characterize this behavior, we measured  $T_c$ ,  $J_c$ , and  $S$  in sample #2 before pressurization and after pressurization to 1.08 GPa, followed by full pressure release. Figure 4(a) compares the temperature-dependent moment in each case, revealing a noticeable increase in  $T_c^{onset}$  for both samples after the pressure cycle, plotted in the inset.

Magnetic hysteresis loops were measured at temperatures of 2–22 K before and after the pressure cycles. The 22 K results are shown in Fig. 4(b), and the remaining curves are provided in Supplementary Fig. S2. A clear second magnetization peak (SMP) is observed between 2–18 K for both before and after pressure cycling. However, a striking change occurs at 22 K, where the SMP fully disappears after the pressure cycle. In the Ba122 family, such as Ni-, K-, and Co-doped compounds, the SMP has been associated with a crossover from collec-

tive (elastic) to plastic vortex creep [34–37], often accompanied by a rhombic-to-square vortex lattice transition [38, 39]. For overdoped P-doped Ba122, however, the SMP has been attributed to vortex lattice dislocations rather than a rhombic-to-square transition [40].

To investigate the disappearance of the SMP, we analyzed the vortex pinning mechanism using the pinning force  $F_p = \mu_0 H J_c$  [41–48]. We first calculated the field-dependent critical current density  $J_c(B)$  using the Bean critical state model [24, 25], shown in Fig. 4(c–d). These results clearly demonstrate that the SMP shifts and flattens after the pressure cycle and ultimately disappears at 22 K. Meanwhile, the overall  $J_c$  increases, indicating enhanced vortex pinning. Next, we plot the normalized pinning force  $f = F_p/F_{p,max}$  against the reduced field  $h = H/H(F_{p,max})$  as shown in Fig. 4(e,f). Here,  $F_{p,max}$  is the maximum pinning force, and  $H(F_{p,max})$  is the field at which this maximum occurs. According to the Dew-

Hughes model, the normalized pinning force for three common pinning cases results in the following function forms [42, 48]:

$$\delta\kappa \text{ point pinning: } f = 3h^2 \left(1 - \frac{2h}{3}\right) \quad (6)$$

$$\text{Normal point pinning: } f = \frac{9}{4}h \left(1 - \frac{h}{3}\right)^2 \quad (7)$$

$$\text{Surface pinning: } f = \frac{25}{16}h^{1/2} \left(1 - \frac{h}{5}\right)^2 \quad (8)$$

The  $\delta\kappa$  point pinning mechanism arises when pinning sites locally modify the Ginzburg–Landau parameter,  $\kappa = \lambda/\xi$ , relative to the bulk value, producing a spatial variation in  $\kappa$  that generates a vortex pinning potential. Here,  $\lambda$  is the penetration depth and  $\xi$  is the coherence length. Normal point pinning is caused by defects such as non-superconducting inclusions or point defects and can be associated with  $\delta T_c$  pinning [47]. As the temperature approaches  $T_c$ , variations in the local transition temperature become increasingly important, creating regions of reduced condensation energy. Surface pinning originates from extended two-dimensional defects, including grain and twin boundaries, stacking faults, and dislocation arrays such as sub-grains. As well as plate-like precipitates, and even the surface of the superconductor.

Figure 4(e–f) shows the  $f(h)$  curves before and after the pressure cycle, plotted together with the three Dew-Hughes pinning models described by Eqs. [6–8]. For temperatures  $T \leq 14$  K, the pinning force  $F_p(H)$  does not exhibit a well-defined maximum, and therefore a meaningful  $F_{p,\max}$  cannot be extracted. For this reason, only the 18 and 22 K data are shown. Before the pressure cycle, both the 18 and 22 K curves closely follow the  $\delta\kappa$  pinning model, consistent with previous studies on the P-doped Ba122 system [47]. This pinning behavior has been suggested to originate from nanoscale inhomogeneity in the dopant distribution, which leads to fluctuations in the electron mean free path [47, 49–51].

After the pressure cycle, the 18 K data remain close to the  $\delta\kappa$  model. However, at 22 K the pinning mechanism changes significantly. For  $h > 1$ , the curve follows the normal point ( $\delta T_c$ ) pinning model. For  $h < 1$ , the 22 K data instead align more closely with the surface pinning model. This suggests that the pressure cycle may introduce extended interfaces or planar defects that enhance vortex pinning at higher temperatures. We also note that at 18 K both before and after the pressure cycle, the  $f$  vs  $h$  data exhibit a plateau near  $h \approx 0.3$ , a feature also reported in Ref. [47] and attributed to strong point pinning. Therefore, the disappearance of the SMP at 22 K may be attributed to a pressure-induced modification of the vortex lattice that changes the pinning mechanism from primarily  $\delta\kappa$  pinning to a mixed combination of  $\delta T_c$  and surface pinning.

Lastly, we calculated the temperature dependence of the critical current density  $J_c(T)$  and the vortex creep

parameter  $S(T)$  extracted from magnetic relaxation measurements. As shown in Fig. 5(a–b), pressure cycling results in a dramatic enhancement of vortex pinning, the critical current density increases by more than a factor of three at 8 K and  $\mu_0 H = 0.5$  T, and remains substantially higher across the full temperature window from 2–14 K. Concomitantly, the creep parameter  $S(T)$  is strongly suppressed, as shown in Fig. 5(c–d). At  $\mu_0 H = 1$  T,  $S$  decreases from  $\sim 0.046$  to  $\sim 0.02$ , and even at 0.5 T the relaxation in sample #2 drops from  $\sim 0.038$  to  $\sim 0.02$  at 8 K. This combination of a tripled  $J_c$  and a more than 40% reduce in creep parameter demonstrates that pressure cycling can simultaneously enhance vortex pinning strength and stability, with the improvements fully retained after pressure release.

## CONCLUSIONS

In summary, we have shown that hydrostatic pressures applied using a compact, off-the-shelf pressure cell can substantially and irreversibly enhance vortex pinning in overdoped  $\text{BaFe}_2(\text{As}_{1-x}\text{P}_x)_2$  single crystals. While pressures up to 1.08 GPa produce only a small suppression of  $T_c$ , they lead to a more than threefold increase in  $J_c$  and over a 40% reduction in the creep parameter  $S$  at 8 K and 0.5 T, with these improvements retained after pressure release at room temperature. Pressure cycling also modifies the pinning landscape, suppressing the second magnetization peak at 22 K and providing evidence for a crossover from predominantly  $\delta\kappa$  pinning to a mixed  $\delta T_c$  and surface pinning. These results establish pressure cycling as a simple route to stabilize enhanced vortex pinning without changing composition or introducing artificial pinning centers.

This work motivates future studies to directly correlate structural changes with enhanced pinning by using high-resolution SEM and TEM on crystals before and after pressure cycling. Moreover, applying this protocol to other iron-based superconductors will help test the generality of irreversible pressure-induced effects and may identify compositions that yield even larger improvements in  $J_c$  and creep suppression under practical operating conditions.

## METHODS

### Crystal Growth

Single crystals of  $\text{BaFe}_2(\text{As}_{1-x}\text{P}_x)_2$  were grown using a two-step self-flux method. Binary precursors  $\text{Ba}_2\text{As}_3$ ,  $\text{Ba}_2\text{P}_3$ , FeAs, and FeP were first synthesized from high-purity elements. These precursors were then mixed with Ba pieces in controlled ratios, sealed in evacuated quartz tubes, and heated to high temperatures. Single crystals were obtained upon slow cooling. The detailed growth sequence and mixture ratios are described in Ref. [52, 53].

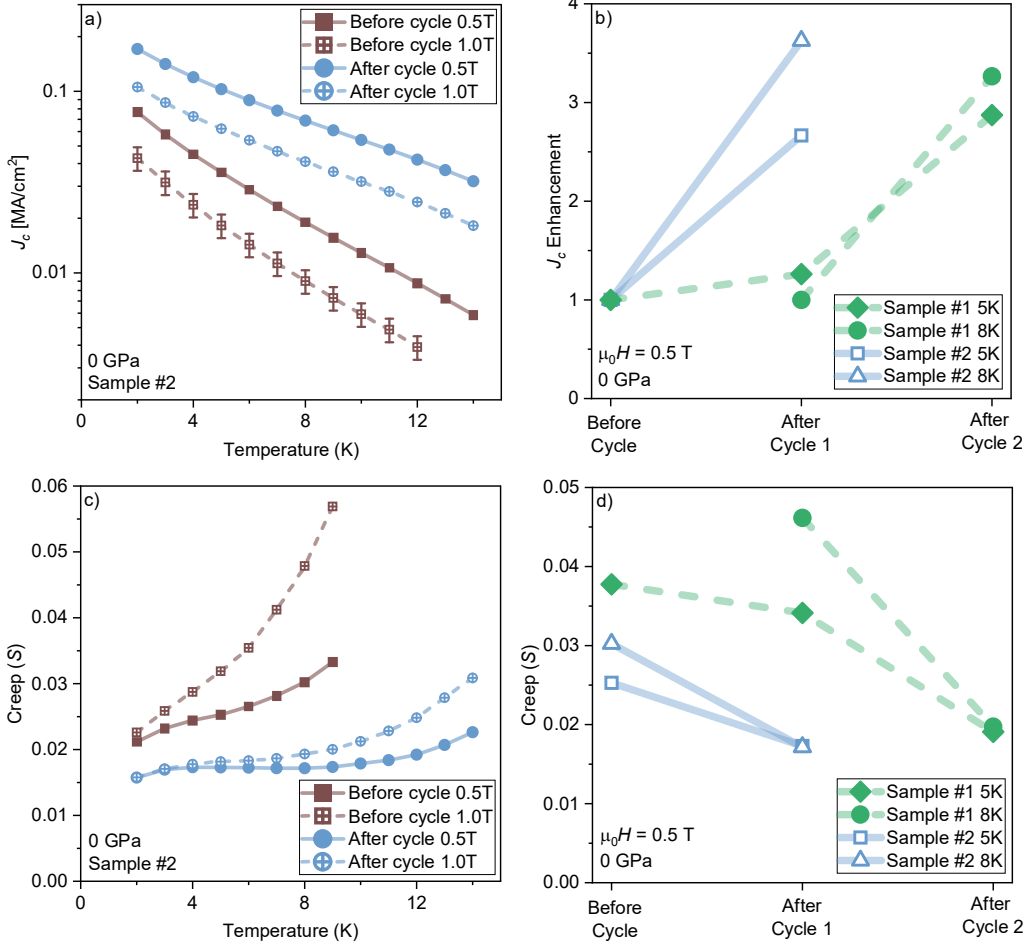


FIG. 5. Temperature-dependent (a)  $J_c$  and (c)  $S$  for Sample #2 measured before and after the pressure cycle under applied fields of  $\mu_0 H = 0.5$  and 1 T. (b) Enhancement of  $J_c$  and (d) the effect of the pressure cycle on  $S$  for both Sample #1 and Sample #2 at 5 K and 8 K under an applied field of  $\mu_0 H = 0.5$  T. Both samples exhibit more than a threefold increase in  $J_c$  at 8 K and 0.5 T after pressure cycling.

Energy-dispersive X-ray spectroscopy (EDS) was used to verify the doping level.

### Magnetometry Measurements

Magnetization measurements were performed using a Quantum Design MPMS3 superconducting quantum interference device (SQUID) magnetometer. Sample #1 was measured inside the Quantum Design high pressure cell module, whereas sample #2 was pressurized using the pressure cell but measured in the standard MPMS3 brass sample holder. The field- and temperature-dependent background signal of the brass sample holder is included in Supplementary Fig. S5. In all measurements, the magnetic field was applied perpendicular to the film plane (parallel to the  $c$ -axis,  $H \parallel c$ ). For mag-

netic hysteresis and relaxation measurements  $m(H)$ , each moment scan was performed over a 25 mm scan length in 4 s, while for moment versus temperature measurements  $m(T)$  used to extract  $T_c$ , a 10 mm scan length collected in 1 s was used.

To determine  $T_c$ , the magnetic moment  $m(T)$  was measured under  $\mu_0 H = 0.2 - 1$  mT while sweeping temperature at approximately  $0.05$  K  $\text{min}^{-1}$  for measurements conducted in the pressure cell and  $1.5$  K  $\text{min}^{-1}$  for measurements using the brass sample holder. Magnetic hysteresis loops  $m(H)$  were acquired by stabilizing the magnetic moment at each field after sweeping at a rate of  $100$  Oe  $\text{s}^{-1}$ .

Magnetic relaxation (vortex creep) was obtained following conventional protocols [28], in which the moment  $m(t, H_1, T_1)$  was recorded every 10 s for approximately one hour after establishing a critical state. The

critical state was established by sweeping the field by  $\Delta H = 2 \text{ T} > 4H^*$ , where  $H^*$  is the minimum flux-penetration field, and then holding the field at  $H_1$  and temperature at  $T_1$ . The preparation of the critical state was confirmed by comparing the initial  $m(t)$  with the corresponding hysteresis loop  $m(H)$ . After subtracting the background contribution from the sample mount and correcting for the time offset between field application and the first recorded point, the creep parameter was extracted using  $S = -d \ln m / d \ln t$  from a linear fit to  $\ln m$  versus  $\ln t$ . The detailed procedure for processing the relaxation data is provided in Supplementary Fig. S3.

## DATA AVAILABILITY

The data supporting the findings of this study are available on Mendeley Data (DOI: 10.17632/j5x7z8nzhy.1) as a zip file. This includes Python code used to process the data and Origin files (.opju) that contain data spreadsheets for all the samples and figures used in this paper, which can be opened using Origin Viewer, a free application that permits viewing and copying of data contained in Origin project files. The code used for pressure cell background

subtraction is adapted from the open source SquidLab program [21].

## ACKNOWLEDGMENTS

This material is based upon work supported by the National Science Foundation under the University of Washington Materials Research Science and Engineering Center under grant DMR-2308979 (J.L., A.L., Z.L., J.C., S.E.).

## AUTHOR CONTRIBUTIONS

S.E. conceived and designed the experiment. Z.L. and J.C. grew the P-doped Ba122 crystals. J.L. performed EDS on crystals. J.L. and A.L. performed magnetization studies and data analysis. J.L. developed the background subtraction procedure and wrote the associated code. S.E. and J.L. thoroughly reviewed the data analysis. J.L. and S.E. wrote the manuscript. All authors commented on the manuscript.

- 
- [1] S. Mandal, R. E. Cohen, and K. Haule, Strong pressure-dependent electron-phonon coupling in fese, *Phys. Rev. B* **89**, 220502 (2014).
- [2] L. Du, S. Hu, Y. Yang, X. Bu, and S. Meng, Correlation-promoted electron-phonon coupling and superconductivity in bulk fese, *Phys. Rev. Mater.* **9**, 114803 (2025).
- [3] B. Lorenz and C. W. Chu, High Pressure Effects on Superconductivity BT - *Frontiers in Superconducting Materials* (Springer Berlin Heidelberg, Berlin, Heidelberg, 2005) pp. 459–497.
- [4] L. N. Sang, Z. Li, G. S. Yang, Z. J. Yue, J. X. Liu, C. B. Cai, T. Wu, S. X. Dou, Y. W. Ma, and X. L. Wang, Pressure effects on iron-based superconductor families: Superconductivity, flux pinning and vortex dynamics, *Materials Today Physics* **19**, 100414 (2021).
- [5] R. Yu, H. Hu, E. M. Nica, J.-X. Zhu, and Q. Si, Orbital Selectivity in Electron Correlations and Superconducting Pairing of Iron-Based Superconductors, *Frontiers in Physics* **Volume 9 - 2021**, 10.3389/fphy.2021.578347 (2021).
- [6] Q. Wu, C. Zhang, B. Li, H. Liu, J. Song, B. Chen, H. Liu, Y. Duan, J. He, J. Liu, G. Cao, and J. Meng, Interplay of electron-phonon coupling, pseudogap, and superconductivity in  $\text{CsCa}_2\text{Fe}_4\text{As}_4\text{F}_2$  studied using ultrafast optical spectroscopy, *Phys. Rev. B* **111**, L081110 (2025).
- [7] E. Gati, L. Xiang, S. L. Bud'ko, and P. C. Canfield, Hydrostatic and Uniaxial Pressure Tuning of Iron-Based Superconductors: Insights into Superconductivity, Magnetism, Nematicity, and Collapsed Tetragonal Transitions, *Annalen der Physik* **532**, 2000248 (2020).
- [8] A. V. Chubukov, M. Khodas, and R. M. Fernandes, Magnetism, superconductivity, and spontaneous orbital order in iron-based superconductors: Which comes first and why?, *Phys. Rev. X* **6**, 041045 (2016).
- [9] T. L. Hung, C. H. Huang, L. Z. Deng, M. N. Ou, Y. Y. Chen, M. K. Wu, S. Y. Huyan, C. W. Chu, P. J. Chen, and T. K. Lee, Pressure induced superconductivity in MnSe, *Nat. Commun.* **12**, 5436 (2021).
- [10] Y. Mizuguchi, F. Tomioka, S. Tsuda, T. Yamaguchi, and Y. Takano, Superconductivity at 27K in tetragonal FeSe under high pressure, *Applied Physics Letters* **93**, 152505 (2008).
- [11] T. Imai, K. Ahilan, F. L. Ning, T. M. McQueen, and R. J. Cava, Why does undoped fese become a high- $T_c$  superconductor under pressure?, *Phys. Rev. Lett.* **102**, 177005 (2009).
- [12] B. Shabbir, X. Wang, S. R. Ghorbani, C. Shekhar, S. Dou, and O. N. Srivastava, Hydrostatic pressure: A very effective approach to significantly enhance critical current density in granular iron pnictide superconductors, *Sci. Rep.* **5**, 8213 (2015).
- [13] B. Shabbir, X. Wang, Y. Ma, S. X. Dou, S. S. Yan, and L. M. Mei, Study of flux pinning mechanism under hydrostatic pressure in optimally doped (Ba,K)Fe<sub>2</sub>As<sub>2</sub> single crystals, *Sci. Rep.* **6**, 23044 (2016).
- [14] L. Sang, B. Shabbir, P. Maheshwari, W. Qiu, Z. Ma, S. Dou, C. Cai, V. P. S. Awana, and X. Wang, Hydrostatic pressure-induced huge enhancement of critical current density and flux pinning in Fe<sub>1-x</sub>Co<sub>x</sub>Se<sub>0.5</sub>Te<sub>0.5</sub> single crystals, *Supercond. Sci. Technol.* **31**, 025009 (2018).
- [15] L. Sang, P. Maheshwari, J. Liu, Z. Li, W. Qiu, G. Yang, C. Cai, S. Dou, V. S. Awana, and X. Wang, In-situ hydrostatic pressure induced significant suppression of magnetic relaxation and enhancement of flux pinning in

- Fe<sub>1-x</sub>Co<sub>x</sub>Se<sub>0.5</sub>Te<sub>0.5</sub> single crystals, *Scr. Mater.* **171**, 57 (2019).
- [16] L. Deng, T. Bontke, R. Dahal, Y. Xie, B. Gao, X. Li, K. Yin, M. Gooch, D. Rolston, T. Chen, Z. Wu, Y. Ma, P. Dai, and C.-W. Chu, Pressure-induced high-temperature superconductivity retained without pressure in FeSe single crystals, *Proceedings of the National Academy of Sciences* **118**, e2108938118 (2021).
- [17] L. Deng, B. Wang, C. Halbert, D. J. Schulze, M. Gooch, T. Bontke, T.-W. Kuo, X. Shi, S. Song, N. Salke, H.-D. Yang, Z. Ren, R. J. Hemley, E. Zurek, R. P. Prasankumar, and C.-W. Chu, Creation, stabilization, and investigation at ambient pressure of pressure-induced superconductivity in Bi<sub>0.5</sub>Sb<sub>1.5</sub>Te<sub>3</sub>, *Proceedings of the National Academy of Sciences* **122**, e2423102122 (2025).
- [18] Quantum Design, Subtracting the sample holder background from dilute samples, <https://qdusa.com/siteDocs/appNotes/1014-213.pdf> (2002), MPMS Application Note 1014-213.
- [19] Quantum Design, Mpms3 .rw.dat file format, <https://qdusa.com/siteDocs/appNotes/1500-022.pdf> (2019), MPMS Application Note 1500-022.
- [20] Quantum Design, Background subtraction using the mpms3, <https://qdusa.com/siteDocs/appNotes/1500-023.pdf> (2019), MPMS Application Note 1500-023.
- [21] M. J. Coak, C. Liu, D. M. Jarvis, S. Park, M. J. Cliffe, and P. A. Goddard, Squidlab—a user-friendly program for background subtraction and fitting of magnetization data, *Rev. Sci. Instrum.* **91**, 023901 (2020).
- [22] L. E. Klintberg, S. K. Goh, S. Kasahara, Y. Nakai, K. Ishida, M. Sutherland, T. Shibauchi, Y. Matsuda, and T. Terashima, Chemical pressure and physical pressure in BaFe<sub>2</sub>(As<sub>1-x</sub>P<sub>x</sub>)<sub>2</sub>, *J. Phys. Soc. Jpn* **79**, 123706 (2010).
- [23] S. K. Goh, Y. Nakai, K. Ishida, L. E. Klintberg, Y. Ihara, S. Kasahara, T. Shibauchi, Y. Matsuda, and T. Terashima, Anisotropic superconducting properties of optimally doped BaFe<sub>2</sub>(As<sub>0.65</sub>P<sub>0.35</sub>)<sub>2</sub> under pressure, *Phys. Rev. B* **82**, 094502 (2010).
- [24] E. M. Gyorgy, R. B. van Dover, K. A. Jackson, L. F. Schneemeyer, and J. V. Waszczak, Anisotropic critical currents in Ba<sub>2</sub>YCu<sub>3</sub>O<sub>7</sub> analyzed using an extended Bean model, *Appl. Phys. Lett.* **55**, 283 (1989).
- [25] E. F. Talantsev and J. L. Tallon, Fundamental nature of the self-field critical current in superconductors, [arXiv:2409.16758](https://arxiv.org/abs/2409.16758) (2024).
- [26] G. Blatter, M. V. Feigel'man, V. B. Geshkenbein, A. I. Larkin, and V. M. Vinokur, Vortices in high-temperature superconductors, *Rev. Mod. Phys.* **66**, 1125 (1994).
- [27] M. V. Feigel'man, V. B. Geshkenbein, A. I. Larkin, and V. M. Vinokur, Theory of collective flux creep, *Phys. Rev. Lett.* **63**, 2303 (1989).
- [28] Y. Yeshurun, A. P. Malozemoff, and A. Shaulov, Magnetic relaxation in high-temperature superconductors, *Rev. Mod. Phys.* **68**, 911 (1996).
- [29] Y. B. Kim, C. F. Hempstead, and A. R. Strnad, Flux creep in hard superconductors, *Phys. Rev.* **131**, 2486 (1963).
- [30] E. Brandt, Thermal fluctuation of the vortex positions in high- $T_c$  superconductors, *Physica C* **162-164**, 1167 (1989).
- [31] M. Buchacek, R. Willa, V. B. Geshkenbein, and G. Blatter, Strong pinning theory of thermal vortex creep in type-II superconductors, *Phys. Rev. B* **100**, 014501 (2019).
- [32] G. Blatter and V. B. Geshkenbein, *Vortex Matter, in The Physics of Superconductors*, edited by K. H. Bennemann and J. B. Ketterson (Springer, 2003) pp. 725–936.
- [33] W.-K. Kwok, U. Welp, A. Glatz, A. E. Koshelev, K. J. Kihlstrom, and G. W. Crabtree, Vortices in high-performance high-temperature superconductors, *Rep. Prog. Phys.* **79**, 116501 (2016).
- [34] S. Sundar, H. S. Amorim, H.-h. Wen, K. A. Yates, L. F. Cohen, and L. Ghivelder, Plastic pinning replaces collective pinning as the second magnetization peak disappears in the pnictide superconductor Ba<sub>0.75</sub>K<sub>0.25</sub>Fe<sub>2</sub>As<sub>2</sub>, *Phys. Rev. B* , 134509 (2017).
- [35] S. Sundar, S. J. Salem-Sugui, E. Lovell, A. Vanstone, L. F. Cohen, D. Gong, R. Zhang, X. Lu, H. Luo, and L. Ghivelder, Doping dependence of the second magnetization peak, critical current density, and pinning mechanism in BaFe<sub>2-x</sub>Ni<sub>x</sub>As<sub>2</sub> pnictide superconductors, *ACS Appl. Electron. Mater.* **1**, 179 (2019).
- [36] Y. Liu, L. Zhou, K. Sun, W. E. Straszheim, M. A. Tanatar, R. Prozorov, and T. A. Lograsso, Doping evolution of the second magnetization peak and magnetic relaxation in (Ba<sub>1-x</sub>K<sub>x</sub>)Fe<sub>2</sub>As<sub>2</sub> single crystals, *Phys. Rev. B* **97**, 054511 (2018).
- [37] Y. Liu, W. Xie, and H. Wen, Thickness dependence of the second magnetization peak effect in Ba<sub>0.6</sub>K<sub>0.4</sub>Fe<sub>2</sub>As<sub>2</sub> single crystals, *Superconductivity* **12**, 100135 (2024).
- [38] B. Rosenstein, B. Y. Shapiro, I. Shapiro, Y. Bruckental, A. Shaulov, and Y. Yeshurun, Peak effect and square-to-rhombic vortex lattice transition in La<sub>2-x</sub>Sr<sub>x</sub>CuO<sub>4</sub>, *Phys. Rev. B* **72**, 144512 (2005).
- [39] S. Sundar, J. Mosqueira, A. D. Alvarenga, D. Sónora, A. S. Sefat, and S. Salem-Sugui, Study of the second magnetization peak and the pinning behaviour in Ba(Fe<sub>0.935</sub>Co<sub>0.065</sub>)<sub>2</sub>As<sub>2</sub> pnictide superconductor, *Supercond. Sci. Technol.* **30**, 125007 (2017).
- [40] L. Miu, A. M. Ionescu, D. Miu, M. Burdusel, P. Badica, D. Batalu, and A. Crisan, Second magnetization peak, rhombic-to-square bragg vortex glass transition, and intersecting magnetic hysteresis curves in overdoped BaFe<sub>2</sub>(As<sub>1-x</sub>P<sub>x</sub>)<sub>2</sub> single crystals, *Sci. Rep.* **10**, 17274 (2020).
- [41] E. J. Kramer, Scaling laws for flux pinning in hard superconductors, *J. Appl. Phys.* **44**, 1360 (1973).
- [42] D. Dew-Hughes, Flux pinning mechanisms in type II superconductors, *Philosophical Magazine* **30**, 293 (1974).
- [43] H. Yamasaki, K. Endo, S. Kosaka, M. Umeda, S. Yoshida, and K. Kajimura, Scaling of the flux pinning force in epitaxial Bi<sub>2</sub>Sr<sub>2</sub>Ca<sub>2</sub>Cu<sub>3</sub>O<sub>x</sub> thin films, *Phys. Rev. Lett.* **70**, 3331 (1993).
- [44] M. R. Koblishka, A. J. J. van Dalen, T. Higuchi, S. I. Yoo, and M. Murakami, Analysis of pinning in NdBa<sub>2</sub>Cu<sub>3</sub>O<sub>7-δ</sub>, *Phys. Rev. B* **58**, 2863 (1998).
- [45] H. Yang, H. Luo, Z. Wang, and H.-H. Wen, Fishtail effect and the vortex phase diagram of single crystal Ba<sub>0.6</sub>K<sub>0.4</sub>Fe<sub>2</sub>As<sub>2</sub>, *Appl. Phys. Lett.* **93**, 142506 (2008).
- [46] A. Yamamoto, J. Jaroszynski, C. Tarantini, L. Balicas, J. Jiang, A. Gurevich, D. C. Larbalestier, R. Jin, A. S. Sefat, M. A. McGuire, B. C. Sales, D. K. Christen, and D. Mandrus, Small anisotropy, weak thermal fluctuations, and high field superconductivity in co-doped iron pnictide Ba<sub>2</sub>(Fe<sub>1-x</sub>Co<sub>x</sub>)<sub>2</sub>As<sub>2</sub> superconductors, *Appl. Phys. Lett.* **94**, 062511 (2009).

- [47] L. Fang, Y. Jia, J. A. Schlueter, A. Kayani, Z. L. Xiao, H. Claus, U. Welp, A. E. Koshelev, G. W. Crabtree, and W.-K. Kwok, Doping- and irradiation-controlled pinning of vortices in  $\text{BaFe}_2(\text{As}_{1-x}\text{P}_x)_2$  single crystals, *Phys. Rev. B* **84**, 140504 (2011).
- [48] H. Luo, X. Wang, X. Zhou, L. Sun, M. Liu, R. Guo, S. Li, Y. Sun, and Z. Shi, Increase of critical current density in FeSe superconductors due to the strain effect, *Supercond. Sci. Technol.* **38**, 115004 (2025).
- [49] C. J. van der Beek, G. Rizza, M. Konczykowski, P. Fertey, I. Monnet, T. Klein, R. Okazaki, M. Ishikado, H. Kito, A. Iyo, H. Eisaki, S. Shamoto, M. E. Tillman, S. L. Bud'ko, P. C. Canfield, T. Shibauchi, and Y. Matsuda, Flux pinning in  $\text{PrFeAsO}_{0.9}$  and  $\text{NdFeAsO}_{0.9}\text{F}_{0.1}$  superconducting crystals, *Phys. Rev. B* **81**, 174517 (2010).
- [50] S. Chong, S. Hashimoto, and K. Kadowaki, Upper critical fields and critical current density of  $\text{BaFe}_2(\text{As}_{0.68}\text{P}_{0.32})_2$  single crystal, *Solid State Commun.* **150**, 1178 (2010).
- [51] B. Shabbir, X. L. Wang, S. R. Ghorbani, S. X. Dou, and F. Xiang, Hydrostatic pressure induced transition from  $\delta T_c$  to  $\delta \ell$  pinning mechanism in  $\text{MgB}_2$ , *Supercond. Sci. Technol.* **28**, 055001 (2015).
- [52] M. Nakajima, S.-i. Uchida, K. Kihou, C.-H. Lee, A. Iyo, and H. Eisaki, Growth of  $\text{BaFe}_2(\text{As}_{1-x}\text{P}_x)_2$  single crystals ( $0 \leq x \leq 1$ ) by  $\text{Ba}_2\text{As}_3/\text{Ba}_2\text{P}_3$ -flux method, *J. Phys. Soc. Jpn.* **81**, 104710 (2012).
- [53] W. Zhang, Y. Wei, T. Xie, Z. Liu, D. Gong, X. Ma, D. Hu, P. Čermák, A. Schneidewind, G. Tucker, S. Meng, Z. Huesges, Z. Lu, J. Song, W. Luo, L. Xu, Z. Zhu, X. Yin, H.-F. Li, Y.-f. Yang, H. Luo, and S. Li, Unconventional antiferromagnetic quantum critical point in  $\text{Ba}(\text{Fe}_{0.97}\text{Cr}_{0.03})_2(\text{As}_{1-x}\text{P}_x)_2$ , *Phys. Rev. Lett.* **122**, 037001 (2019).

## SUPPLEMENTAL MATERIALS

### PRESSURE CALIBRATION

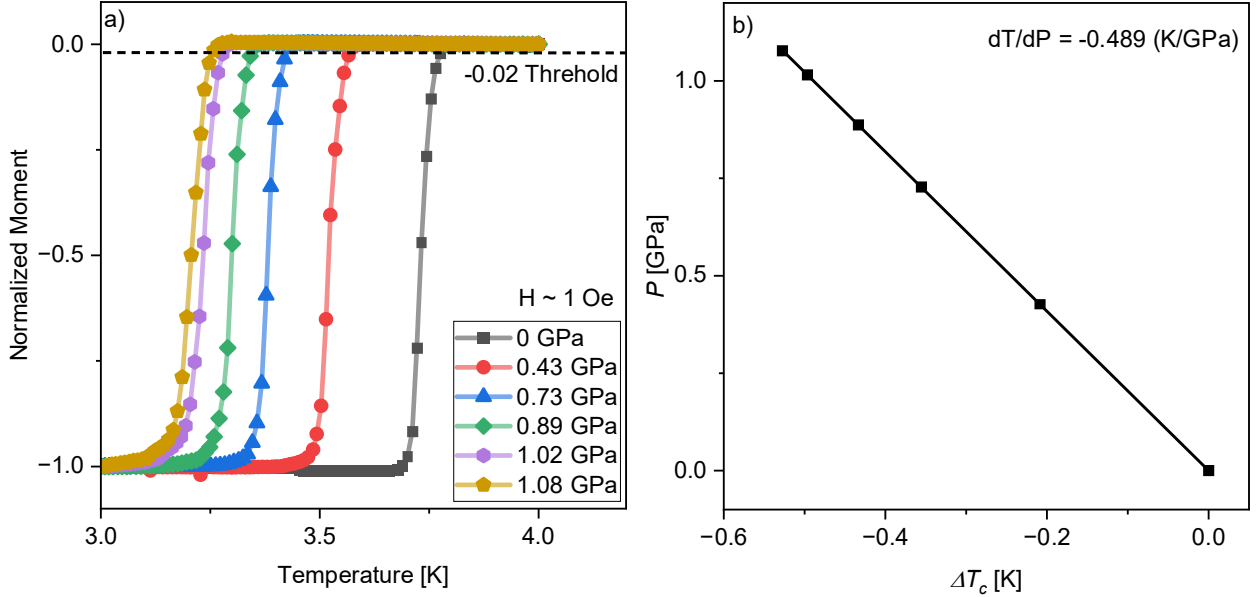


FIG. S1. (a) Normalized moment against temperature for the tin manometer at different pressures. (b) Pressure against  $\Delta T_c = T_c - T_c(0 \text{ GPa})$ . Using the linear pressure dependent on tin  $dT_c/dP = -0.489 \text{ K/GPa}$ , pressure can be calculated using  $P = \Delta T_c / (-0.489)$ .

A moment against temperature measurement was performed on the tin manometer between 3–4 K under zero field cooled conditions to determine its  $T_c$ . The  $T_c$  is defined as the temperature at which the normalized magnetic moment drops below the threshold value of  $-0.02$ , as shown in Fig. S1(a). The applied pressure is then calculated using  $P = \Delta T_c / (-0.489)$ , where  $\Delta T_c = T_c - T_c(0 \text{ GPa})$ , as shown in Fig. S1(b).

## MAGNETIC HYSTERESIS

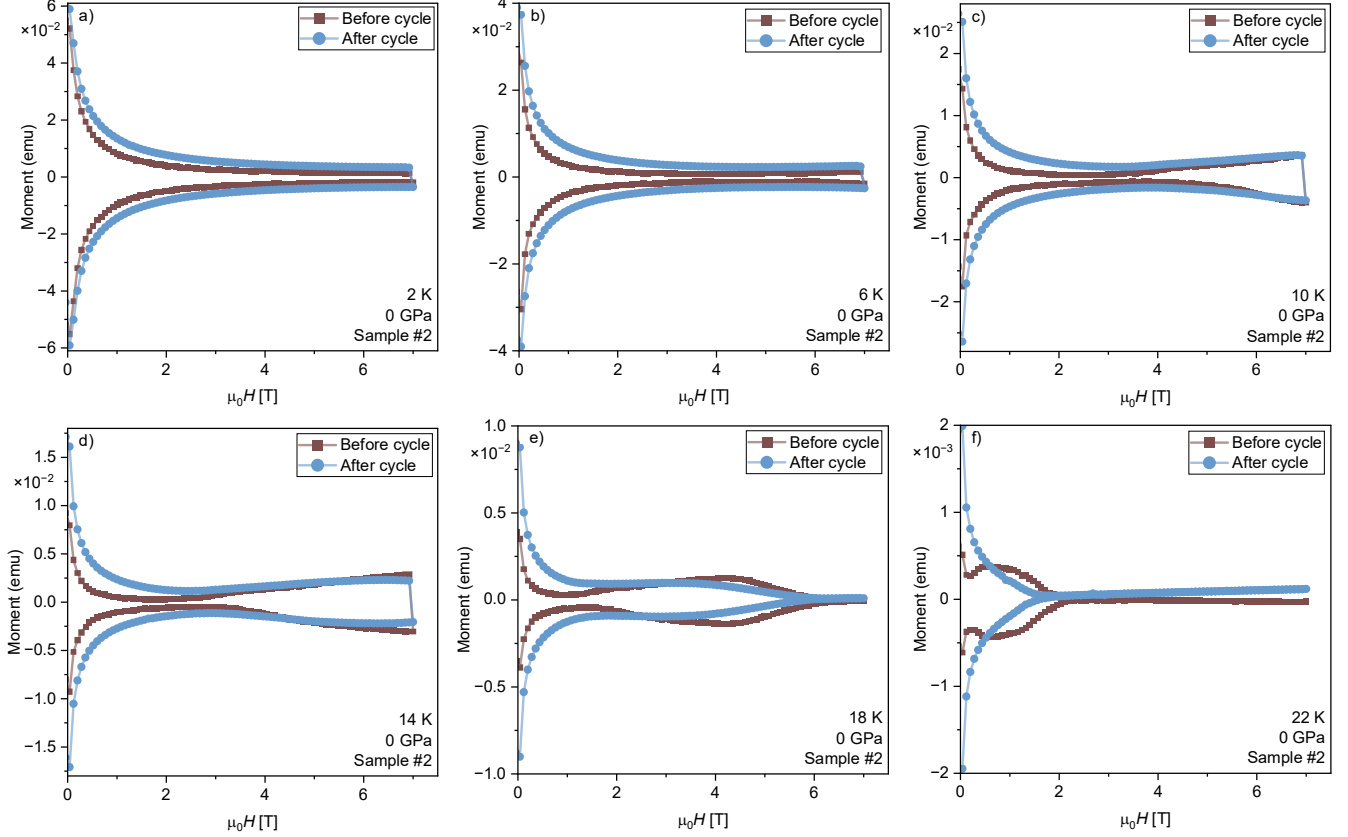


FIG. S2. Effect of the pressure cycle on the magnetic hysteresis loop of Sample #2 at (a) 2 K, (b) 6 K, (c) 10 K, (d) 14 K, (e) 18 K, (f) 22 K.

Magnetic hysteresis loops measured before and after the pressure cycle for sample #2 between 2 and 22 K are shown in Fig. S2(a–f). For temperatures between 2 and 10 K, the pressure cycle increases the magnetic moment across all applied fields. At intermediate temperatures 14 – 18 K, before the second magnetization peak (SMP), the pressure cycle enhances the moment, whereas above the SMP, the moment is reduced after pressure cycling. We also observed that the SMP shifts to lower fields, as seen in Fig. S1(d, e). At 22 K, the SMP disappears entirely, as shown in Fig. S1(f).

## MAGNETIC RELAXATION

Figure S3(a) shows the example raw magnetic relaxation data for sample #2 after the first pressure cycle, measured under an applied field of  $\mu_0 H = 1$  T. Relaxation was recorded for 5 minutes on the lower branch and for 60 minutes on the upper branch of the hysteresis loop, in both cases after preparing the sample in the critical state. Because the MPMS3 acquires the first data point after a short delay, during which relaxation has already begun. Therefore, we introduce a system delay time  $t_d$  when extracting the vortex creep rate. The creep parameter is defined as  $S = -d \ln m / d \ln(t + t_d)$ , where  $t_d$  is treated as a fitting parameter chosen to maximize the linear correlation. The fully processed moment data used to obtain  $S$  are shown in Fig. S3(b).

Figure S4(a) presents additional results of the temperature dependence of  $J_c$  at  $\mu_0 H = 1$  T for sample #1, calculated using the Bean model from the initial magnetization value in the relaxation measurement. Figure S4(b) shows the corresponding temperature dependence of the vortex creep parameter  $S$  for sample #1.

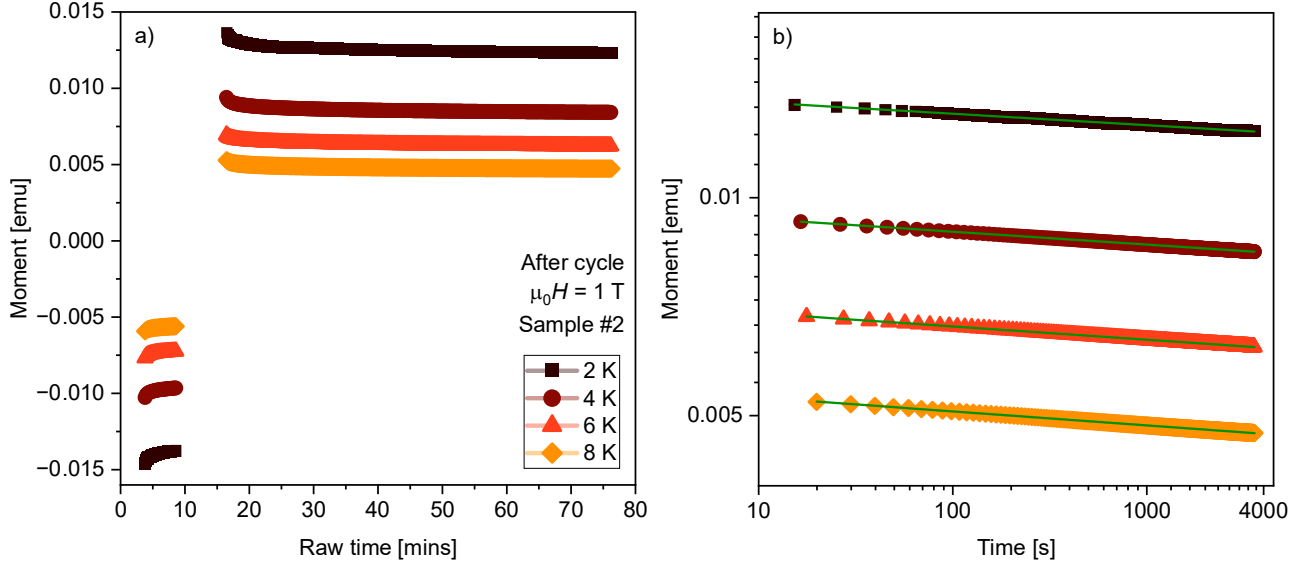


FIG. S3. (a) Example raw magnetic relaxation curves  $m(t)$  for sample #2 after the first pressure cycle, measured at  $\mu_0 H = 1$  T for various temperatures. (b) The same data after correcting for the system delay time  $t_d$ . The resulting plots show  $\ln m$  versus  $\ln(t + t_d)$ , where the slope of the linear fit defines the relaxation rate  $S$ .

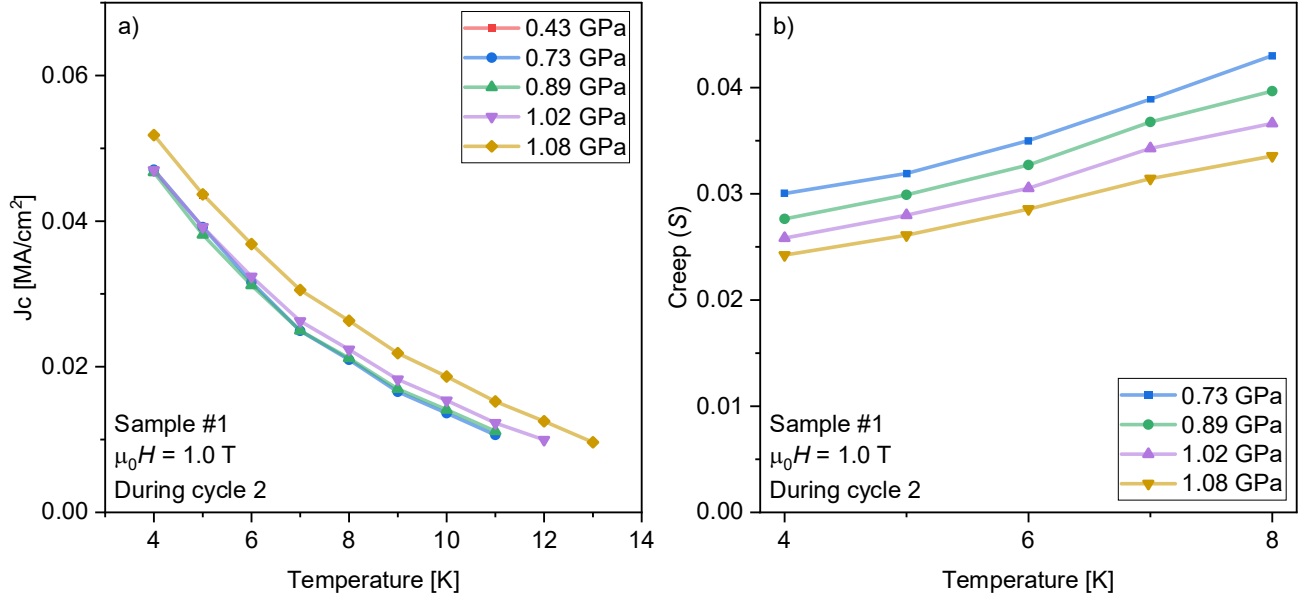


FIG. S4. (a) Critical current density  $J_c$  as a function of temperature for sample #1 during pressure cycle 2 at  $\mu_0 H = 1$  T. Here,  $J_c$  is calculated using Bean's critical state model from the first data point of the magnetic relaxation measurement. (b) Vortex creep parameter  $S$  as a function of temperature for sample #1 during pressure cycle 2 at  $\mu_0 H = 1$  T.

## MAGNETIC BACKGROUND OF MPMS 3 BRASS SAMPLE HOLDER

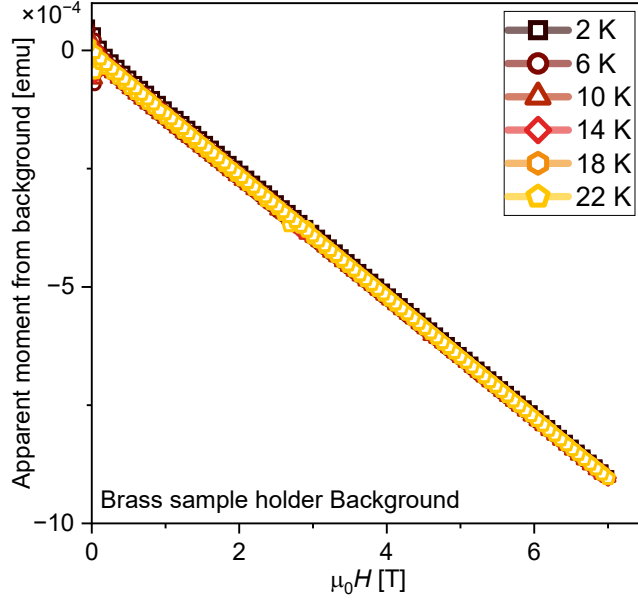


FIG. S5. Field-dependent background moment of the brass sample holder measured at different temperatures. The “apparent moment” refers to the moment parameter returned by the dipole fit applied to a non-dipolar background response.

Sample #1 was measured using the pressure cell module, whereas sample #2 was measured using the brass sample holder. It is therefore important to characterize the background signal of the brass sample holder. The brass sample holder exhibits a much weaker background, showing a linear field dependence and reaching only about  $9 \times 10^{-4}$  emu at 7 T. In addition, it shows no measurable temperature dependence between 2 and 22 K. Although the background moment is small, to maintain consistency across all measurements in this study, voltage–position background subtraction was also performed for all data collected using the brass sample holder.

TABLE S1. Sample dimensions.

sample #	After Cycle number	length $l$ mm	width $w$ mm	thickness $\delta$ $\mu\text{m}$
1	1	$0.981 \pm 0.231$	$0.93 \pm 0.162$	$46.12 \pm 3.65$
2	0	$1.283 \pm 0.077$	$1.068 \pm 0.069$	$74.78 \pm 8.21$
2	1	$1.229 \pm 0.122$	$0.997 \pm 0.157$	$57.17 \pm 6.78$